Materials
Horizons

ROYAL SOCIETY
OF CHEMISTRY

COMMUNICATION

View Article Online
View Journal

Check for updates

Cite this: DOI: 10.1039/d0mh01359e

Received 21st August 2020,
Accepted 8th December 2020

DOI: 10.1039/d0mh01359e

rsc.li/materials-horizons

Sensing arbitrary contact forces with a flexible porous dielectric elastomer†

Baoqing Nie, [a] Jialei Geng,[a] Ting Yao,[a] Yihui Miao,[a] Yiqiu Zhang,[b]
Xinjian Chen*[ac] and Jian Liu *[b]

Artificial tactile sensing in next-generation robots requires the development of flexible sensors for complicated tactile force measurements in both normal and tangential directions. A variety of microstructures have been proposed to be integrated with material development for the enhanced performance of the devices. However, there remains a great challenge in this field on how to decouple contact forces in spatially arbitrary directions with the electric signal readouts. The fundamental correlation between contact force sensing and the microstructure deformations is still largely unknown. Here, we report a new method of arbitrary force deconvolution and sensitive detection of flexible contacts by a porous dielectric elastomer-based force (PDiF) sensor. Decoupling the complicated nonlinear mathematic problem reveals a critical synergy in the porous elastomer between the electrical property enhancement and the geometrical deformations induced by arbitrary contact forces. Proof-of-concept applications in flexible tactile sensing have been demonstrated with the PDiF sensors, including surface roughness discrimination, slippage detection, and real-time force mapping in handwriting. It creates an avenue for flexible sensing of the complicated contact forces with microstructure-embedded elastomeric materials.

New concepts

Flexible pressure sensors have emerged with important applications in wearable electronics. A variety of microstructures have been proposed to be integrated with material development for enhanced performance of the devices. However, there remains a great challenge in this field on how to decouple arbitrary contact forces with the electric signal readouts. Few reports in the literature provide a clear solution to the fundamental correlation between contact force sensing and the microstructure deformations. In this study, we report a new method of arbitrary force deconvolution and sensitive detection of flexible contacts by a porous dielectric elastomer-based force (PDiF) sensor. Besides the significantly improved performance in force sensing, this device has inspired us to develop a unique mathematic model to solve the nonlinear problem of contact force deconvolution. Our study defines this problem of force deconvolution correlated to the deformations of dielectric microstructures, but also brings an effective and straightforward solution to it. This work highlights the effectiveness of constructing arbitrary force sensors based on a porous dielectric elastomer with a straightforward force deconvolution model, providing a new route for flexible sensing of the complicated contact forces with microstructure-embedded elastomeric materials.

Introduction

Artificial tactile sensing emerges with a wide range of flexible electronics, including soft electrodes, flexible sensors, wearable energy generators and memristor devices.[1–6] Among those state-of-the-art electronics, flexible force/pressure sensors are required to simultaneously detect both the normal and the tangential loads onto the sensor surface.[7–10] A variety of sensing principles have been examined for the detection of three-dimensional (3D) loads, including piezoelectric, resistive, capacitive, and optical techniques.[11–14] Resistive force sensing has been proposed by employing a number of electrically conductive materials. For instance, conductive rubber or metal is being developed to respond to an external force in any arbitrary direction with the compression or stretching of the built-in conductive element by resistance changes.[15–17] Nevertheless, there still exist several major technical limitations in those techniques, including complexity in device fabrication, liability to thermal fluctuations, and the crosstalk among the units for sensing multi-dimensional forces. Alternatively, capacitive sensing is attractive in this field due to its high sensitivity, low power consumption, and immunity to thermal noise.[18] Force sensors in the classic parallel-plate configuration allow for the measurement of a normal load or a shear stress by the changes

---

[a] *School of Electronic and Information Engineering, Soochow University, Suzhou, Jiangsu 215006, China. E-mail: xjchen@suda.edu.cn*

[b] *Institute of Functional Nano and Soft Materials, Jiangsu Key Laboratory for Carbon-Based Functional Materials and Devices, Soochow University, Suzhou, Jiangsu 215123, China. E-mail: jliu@suda.edu.cn*

[c] *State Key Laboratory of Radiation Medicine and Protection, Soochow University, Suzhou 215123, China*

† Electronic supplementary information (ESI) available. See DOI: 10.1039/d0mh01359e

of the separation distance and the overlapping surface areas between the electrode plates.[19–22]

Elastic polymers, such as soft silicone rubbers (*e.g.*, polydimethylsiloxane or PDMS, Ecoflex), adaptable hydrogels and flexible fabrics serve as good candidate materials in the development of wearable electronics.[23–27] Their advantages typically include being soft and robust, versatile synthesis methods for mass production, and prominent biocompatibility.[28] Researchers have been actively trying to promote the performance of the devices built on these materials by various methods, such as hybridizing different polymers, tailoring nano-scaled configurations, and developing micro-structures on the surface or in the bulk of polymeric materials.[29–33] Mu *et al.* reported a resistive sensor built on porous PDMS hybridizing carbon nanotubes and graphene oxide nanosheets as an artificial skin. It allowed for the sensitive detection of tangential forces, but the sensitivity varied along with the changes of the normal forces.[17] Beccai *et al.* introduced a two sub-layered air/PDMS composite dielectric into the sensor for sensitivity enhancement. However, the missing bit of appropriate decoupling resulted in a crosstalk between the detection threshold in the tangential direction and the magnitude of the normal force, accompanied by large measurement errors.[9] Most reports in the

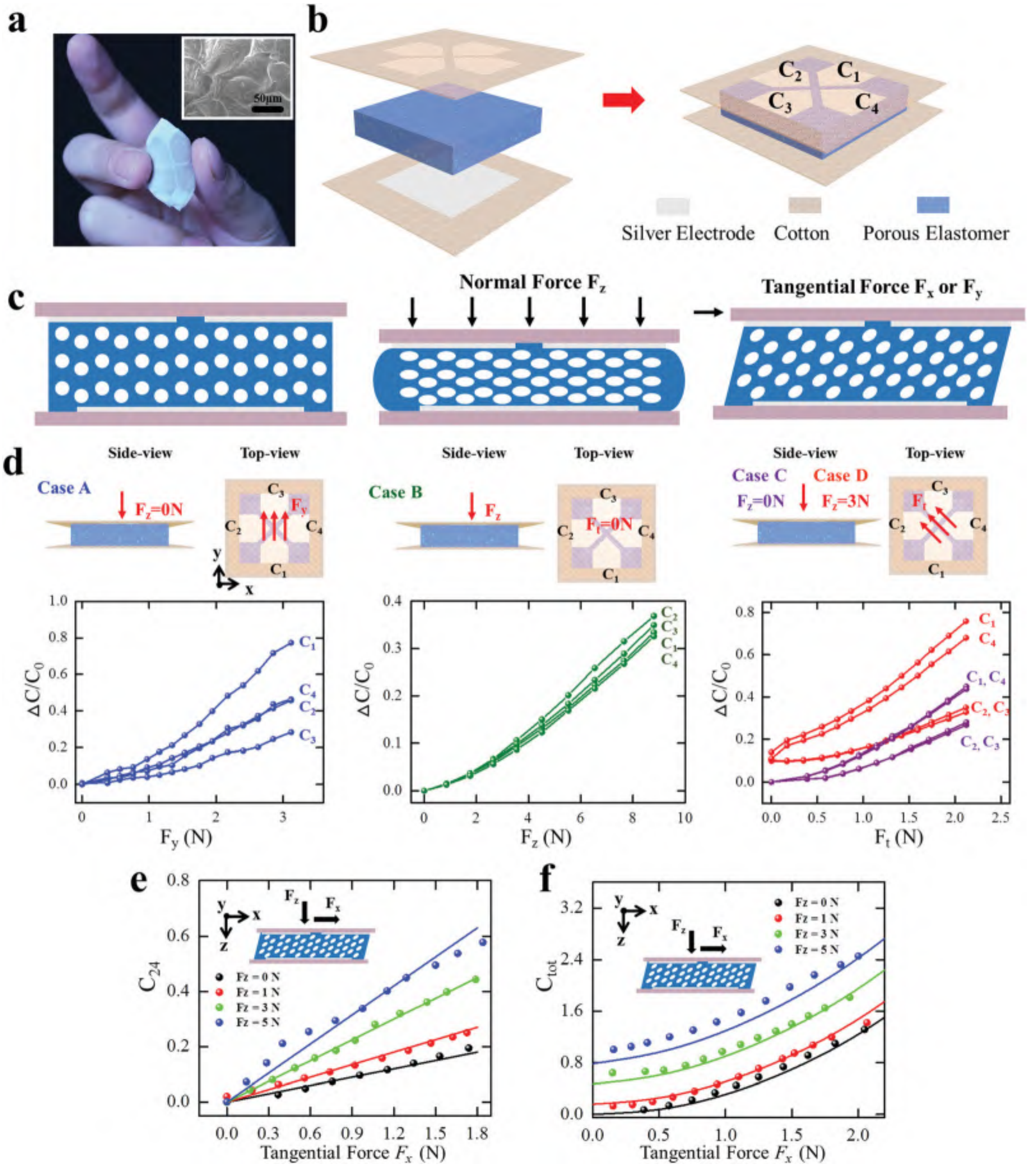

Fig. 1 (a) Photograph of a porous dielectric elastomer-based force (PDiF) sensor. Inset shows a scanning electron microscope (SEM) image of the micro-porous elastomer layer. (b) Schematic illustration of the assembly and the structure of the PDiF sensor. (c) Schematic deformations of the porous elastomer under a normal force or a tangential force in the cross-sectional view. (d) Schematic illustrations of the PDiF sensor under different external forces, including one force component (F_y in Case A and F_z in Case B), two components (F_x and F_y in Case C), and three directions (F_x, F_y and F_z, Case D), along with the corresponding relative capacitance changes ($\Delta C/C_0$) of the four sensing units in the four cases (color-coded). F_t equals $\sqrt{F_x^2 + F_y^2}$. (e and f) The differential capacitance C_{24} defined in eqn (5) and the total capacitance change C_{tot} defined in eqn (6) of the sensor against tangential loads (F_x) under various normal forces (F_z). Dots: the experimental data by measurements; solid lines: the fitting values from eqn (5) and (6).

literature focus on how to improve the device performance further, but lack the methodology for the deconvolution of forces in arbitrary directions. A few articles involving neural network algorithms for force decoupling suffer from the limitation of a black-box view of the algorithm, it thus being difficult to explain the mechanism of force–electric correlation in those devices.[34] As the sensor structures become more complicated by interlocking micro domes,[16] nanofiber hairs,[35] micro burrs,[36] or air pores,[17] it increasingly raises a fundamental challenge on how to decouple the forces in arbitrary directions.

Herein, we propose a porous dielectric force (PDiF) sensor for the detection of contact forces in spatially arbitrary directions (abbreviated as arbitrary contact forces, Fig. 1a and b, and Fig. S1 and S2, ESI†). It consists of two flexible cotton layers with conductive patterns and a dielectric elastomer film with a porous network. Implementing four parallel plate capacitors on the porous elastic film allows for resolving both normal and tangent mechanical loads to the surface. The porous structure in the dielectric layer reduces the Young's modulus and increases the effective dielectric constant under compression, synergistically promoting the sensitivity. Interestingly, both the normal and tangential loads can deform the pores, thus enabling a nonlinear amplification of the capacitive outputs. We have specifically developed a unique mathematic model to solve the nonlinear problem by a linear regression approach, and revealed the mechanism of arbitrary contact force sensing through the changes of the porous structures in the dielectric layer. Our PDiF sensor achieves a sensitivity of 0.16 N^{-1} and 0.10 N^{-1} with minimal detectable forces of 100 mN and 40 mN, in the normal and tangential directions, respectively. The porous elastomer sensor provides an outstanding response/recovery time on the order of a hundred milliseconds. The PDiF sensor has been successfully demonstrated for several important proof-of-concept applications, including identification of various surfaces with different roughnesses, detection of the slippage of hand-held objects, and real-time mapping of the force change patterns in handwriting recognition, which promises great potential in the development of flexible artificial skins.

Results

Capacitive responses to arbitrary contact forces

Fig. 1c illustrates the working principle of the PDiF sensor in a cross-sectional view. The top fabric layer contains the silver ink/cotton composite in a four-leaf-clover-like pattern, with each leaf representing an independent electrode. The bottom fabric layer is composed of the same material in a large, square pattern to serve as the common electrode. The two fabric layers sandwich an elastic dielectric film with micro-scaled pores. In this design, four parallel-plate capacitive units are assembled simultaneously. The capacitance in each unit (C) follows:

$$C = \varepsilon S/d \tag{1}$$

where ε is the permittivity of the porous dielectric material. S and d are the overlapping areas and the distance defined by the top and bottom electrodes, respectively.

As a normal force (F_z) is applied on the PDiF sensor surface, the dielectric layer deforms in the z-axis direction. The distance of the top and bottom electrodes (d) decreases, producing detectable enhancements in the four capacitors. Importantly, the normal mechanical load on the dielectric layer leads to compression of the pores, which further promotes the capacitance changes by increasing the permittivity of the dielectric layer (ε). In an alternative case, an in-plane force in the x-axis (F_x) or y-axis (F_y) direction applied on the sensor surface introduces a shear strain on the porous dielectric layer. The elastic deformation changes the overlapping areas between the top and bottom electrodes (S) along the force loading direction, thus generating differential capacitance among the individual units of the sensor.

Fig. 1d illustrates the relative capacitance changes ($\Delta C_n/C_n^0$, $n = 1, 2, 3$ and 4, C^0 is the initial capacitance) of the four sensing units, when the external forces with either one force component (F_y or F_z, Case A or B), two components (F_x and F_y, Case C), or three dimensional components (F_x, F_y and F_z, Case D) are applied to the PDiF sensor. As shown in Case A, under the in-plane force along the y-axis, the relative capacitance changes in the four units all increase from the initial value ($C_n^0 = 3.3$ pF on the average) to different extents. For instance, the capacitance of C_1 and C_3 is increased by 77.2% and 28.3% respectively, as the tangential force F_y changes from 0 to 3.2 N. The capacitance of C_2 and C_4 is increased by 45% under the identical force range. This effect is mainly attributed to two factors: (1) the tangential forces change the overlapping areas of the top and bottom electrodes; (2) the pores inside the dielectric elastomer are stretched by the tangential forces, leading to the increase of the dielectric constant ε. The first factor results in differential capacitances between the two opposite units, while the second leads to capacitance increases in all the units. As a normal force F_z up to 9 N is applied, all the four capacitances increase by 34% on average (Case B). When the PDiF sensor is taken as an in-plane force with two components (F_x and F_y in equal magnitude) in Case C, the capacitance changes of the four units can be divided into two groups depending on the overlapping areas. C_1 and C_4 in group I exhibit a larger increase (by 40.5%) than C_2 and C_3 in group II (by 20.6%) under the force of 2 N. Interestingly, in Case D, when a normal force (3 N) and a tangential force (0–2.1 N) are superimposed simultaneously, the capacitance changes of the four units are in the same group (C_1 and C_4 in group I, and C_2 and C_3 in group II), except that the initial capacitance values in all units jump equally (by 10%) in response to the normal force component (3 N). All of the results consistently match the rules mentioned as above.

Development of a mathematical model for arbitrary contact force decoupling

We have developed a coefficient matrix A between the arbitrary forces and the capacitance outputs, in order to determine the transduction principle mediated by the porous dielectric elastomer. Specifically, we use the least squares method to reconstruct the coefficient matrix based on the data sets of ($\Delta C_1/C_1^0$, $\Delta C_2/C_2^0$, $\Delta C_3/C_3^0$, $\Delta C_4/C_4^0$, F_x, F_y, F_z) from a large number of independent measurements (total number of experiments, $n = 167$). Eqn (2) and (3) illustrate the matrix A which defines the fundamental transduction principle between the forces and the capacitance outputs. Fig. S4 (ESI†) presents a comparison of the experimental data (blue dots) and fitted values (red dots). Accordingly, the least-square algorithm offers an excellent prediction indicated by the root mean squared error of 0.033. More details on the analysis of the relationship of capacitive outputs and forces are available in the ESI.†

$$\begin{bmatrix} \Delta C_1/C_1^0 \\ \Delta C_2/C_2^0 \\ \Delta C_3/C_3^0 \\ \Delta C_4/C_4^0 \end{bmatrix} = A \cdot \begin{bmatrix} F_x & F_y & F_z & F_x^2 & F_y^2 & F_xF_z & F_yF_z \end{bmatrix}' \tag{2}$$

where the matrix A is defined as:

$$A = \begin{bmatrix} 0 & 5 & 3.9 & 7.7 & 7.7 & 0 & 4.5 \\ 5 & 0 & 3.9 & 7.7 & 7.7 & 4.5 & 0 \\ 0 & -5 & 3.9 & 7.7 & 7.7 & 0 & -0.5 \\ -5 & 0 & 3.9 & 7.7 & 7.7 & -0.5 & 0 \end{bmatrix} \times 10^{-2} \tag{3}$$

Therefore, the forces and capacitance can be predicted by the following equations:

$$C_{13} = (\sigma_t + m \times F_z) \times F_y \tag{4}$$

$$C_{24} = (\sigma_t + m \times F_z) \times F_x \tag{5}$$

$$C_{\text{tot}} = [\sigma_n + n \times (F_x \times F_y)] \times F_z + p \times ({F_x}^2 + {F_y}^2) \tag{6}$$

where $\sigma_t = 0.10$, $\sigma_n = 0.157$, $m = 0.05$, $n = 0.04$ and $p = 0.31$. C_{13}, C_{24} and C_{tot} are defined as:

$$C_{13} = \Delta C_1/C_1^0 - \Delta C_3/C_3^0 \tag{7}$$

$$C_{24} = \Delta C_2/C_2^0 - \Delta C_4/C_4^0 \tag{8}$$

$$C_{\text{tot}} = \Delta C_1/C_1^0 + \Delta C_2/C_2^0 + \Delta C_3/C_3^0 + \Delta C_4/C_4^0 \tag{9}$$

Combining eqn (7)–(9) with eqn (1), there are:

$$C_{13} \text{ (or } C_{24}) = 2 \times (\varepsilon/\varepsilon^0) \times (d^0/d) \times (\Delta S/S^0) \tag{10}$$

$$C_{\text{tot}} = 4 \times [(\varepsilon/\varepsilon^0) \times (d^0/d) - 1] \tag{11}$$

Different from the permittivity of a solid elastomer, the term of $\varepsilon/\varepsilon^0$ in eqn (10) and (11) represents the permittivity change of the porous Ecoflex, which is a function of F_x, F_y and F_z. Additionally, d^0/d or $\Delta S/S^0$ indicates the distance or overlapping area change between the top and the bottom electrodes, which is determined by the normal force F_z or the tangential force (F_x or F_y) respectively. According to eqn (4)–(6), and (10) and (11), we can conclude that: (1) if only the normal force F_z is applied, $\Delta S/S^0$ equals to zero. C_{tot} is linear to F_z; (2) if only the tangential force is applied, the term d^0/d equals to 1. C_{13} and C_{24} are proportional to F_y and F_x, respectively. In addition, due to the presence of the porous structure, the tangential force would induce the change in $\varepsilon/\varepsilon^0$ in eqn (11), in consequence, leading to C_{tot} correlated to the quadratic terms of ${F_x}^2 + {F_y}^2$; (3) if an arbitrary contact force including both normal and tangential components is applied onto the sensor, all the three terms $\varepsilon/\varepsilon^0$, d^0/d and $\Delta S/S^0$ vary with the force. As a result, the capacitive outputs, *i.e.*, C_{13}, C_{24} and C_{tot}, are subject to the synergistic effect of the force components, *i.e.*, $F_y \times F_z$ or $F_x \times F_z$. Although the porous structure in the dielectric elastomer brings a complicated nonlinear problem of force decoupling, we have successfully solved it through implementing the coefficient matrix with a regression method. It features a high efficiency of calculation in comparison to the neural network-based decoupling methods,[34,37] but also provides straightforward clues of understanding the mechanistic impact of the porous structures on the arbitrary contact force sensing.

Fig. 1e and f present the sensor responses (C_{13}, C_{24} and C_{tot}) against the normal (F_z) and tangential (F_x or F_y) forces (dots: experimental measurements, lines: theoretical calculation based on the above equations). As predicted, the differential capacitance C_{24} shows a linear response to the tangential load (F_x) under a constant normal force (Fig. 1e). Here the tangential sensitivity σ_t, defined as C_{24}/F_x, is increased from 0.10 N^{-1} to 0.34 N^{-1} as the normal load increases to 5 N. In Fig. 1f, the total capacitance changes of all four units C_{tot} are governed by both F_z and F_x, suggesting a synergetic effect between the normal and tangential force components on the four units consistent with the prediction by eqn (6). There is a nonlinear relationship between C_{tot} and F_x, in the condition of constant F_z. The value of C_{tot} is increased from 1.3 to 2.5 as F_z rises from 0 to 5 N under the tangential load of 2 N.

Comparison of solid and porous elastomers

As revealed in eqn (1), the capacitance of a parallel-plate capacitor is determined by the separation distance between the electrodes (d), the overall lapping area (S) and the effective dielectric constant of the porous dielectric layer (ε). According to the design of the PDiF sensor, the presence of the pores in the elastomeric assembly makes the force-sensing material softer. Consequently, the porous dielectric elastomer can undergo a larger deformation under the same amount of external load, in comparison to the solid elastomer. In addition, under external compression, the pores get gradually closed and the air fraction in the elastomeric assembly reduces, leading to an effective increase in the dielectric constant ε. All these factors contribute to the high sensitivity of the PDiF sensor.

We have performed experiments for comparison of the dielectric properties and mechanical behaviors of the porous and solid elastomeric materials. Fig. 2a and b illustrate the photographs and SEM images of the elastomers without and with pores. The SEM images suggest that many pores are connected to each other by the channels of various shapes (marked in blue). There might exist some pores with a closed-cell structure (marked in the red), which should be treated with caution because the cross-section view cannot reveal all the hidden channels. Therefore, the pores in the elastomer layer are dominantly featured with open-cell structures. Additionally,

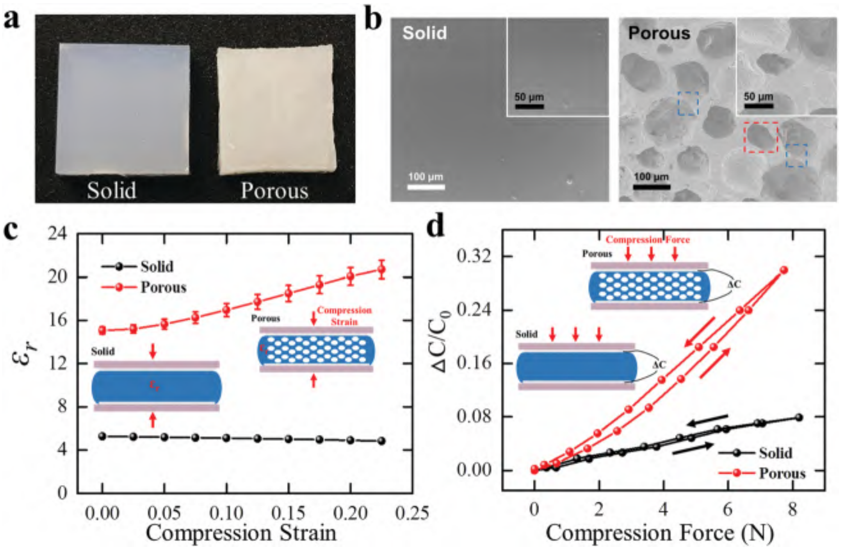

Fig. 2 The performance comparison of the sensors using a solid or porous dielectric elastomer. (a and b) Photograph and SEM images of the dielectric elastomers without or with porous structures. Closed-cell or open-cell pores are marked in red or blue boxes, respectively. (c) Comparison of the dielectric constant variations between the solid and porous elastomers. (d) Relative capacitive changes in response to a normal load using these two different types of elastomers.

the Young's modulus is largely reduced by introducing the pores (Fig. S5a, ESI†). Fig. 2c compares the relative permittivity ε_r ($\varepsilon_r = \varepsilon/\varepsilon_v$, where ε_v is the vacuum permittivity) variations of the two samples under mechanical compression. As for the solid elastomer, the effective dielectric remains a constant of ~5 in the entire compression range. In contrast, the dielectric constant of the porous elastomer is increased by 35.58% in the identical conditions. The difference is attributed to the deformation of the pores, which drives the air out of the elastomer and increases the overall dielectric constant. In addition, the relative permittivity of the porous dielectric drops with the increase of the excitation frequency (Fig. S5b, ESI†). The presence of the pores enlarges the capacitance changes under a compression load, as measured in Fig. 2d. The capacitance change $\Delta C/C_0$ in the sensor with a porous elastomer is 2.9 times larger than the one in the solid elastomeric device under compression forces.

Limit of detection, reproducibility, and response/recovery time

We have performed time-resolved experiments to determine the minimum detectable forces in both the normal and tangential directions. The relative capacitance changes are recorded at a sampling frequency of 5 Hz (Fig. 3a and b) from a single sensing unit. There appear detectable capacitance changes $\Delta C/C_0$ of 0.21% under a normal force of 0.1 N or 0.25% under a tangential force of 0.04 N, respectively. The response/recovery time can be determined by analysis of the capacitive outputs under press and release cycles. The time-resolved relative capacitive changes ($\Delta C/C_0$) and applied normal forces are presented in Fig. 3c. The on/off response time, defined as the duration when the sensor reached 90% of the plateau/valley values, was 0.16 s and 0.37 s, respectively (Fig. 3d). In addition, we have validated the reproducible performance of the PDiF sensor by applying different mechanical loads in the normal direction, varying from 0 to 5.4 N. For all the levels of mechanical loads, the sensor is able to sensitively respond to the dynamic loads and return to its original value (Fig. 3e). The results suggest an excellent reproducibility of our sensor within the applied force ranges. To further evaluate the dynamic response of our sensor, we have measured the capacitance changes as a cyclic force with a varying frequency (0.25, 0.5 and 1 Hz). As shown in Fig. 3f, the amplitudes of the capacitance changes do not decrease by varying the frequency. The results indicate that our sensor can detect dynamic stimuli with periodic change as fast as 1 Hz.

Evaluation of the PDiF sensor in various tactile scenarios

Touching and sensing of the roughness of object surfaces is essential for human skin. Several reports suggest that microscale wrinkles as small as a few microns on the surface can be detected by fingertip.[38] Here, we attempt to test the PDiF sensor for the detection of the surface roughness of planar sheets. Fig. 4a illustrates the test setup. After immobilization of the PDiF sensor on the bottom of a weight (500 g), the device is placed on the testing surface. The weight ensures a constant normal load, generating sufficient friction between the sensor and the testing surface. Fig. 4b illustrates the photographs of two representative surfaces, *i.e.*, a PMMA plate (smooth) and a sandpaper sheet (coarse). The SEM images (Fig. 4c) indicate that the roughness of the PMMA surface is below the scale of microns, while the sandpaper surface features typical particles or wrinkles on the order of hundreds of micrometers. The tangential sensitivity of the sensor is calibrated to be ~0.34 $\mathrm{N^{-1}}$ under the normal load of 500 g (Fig. 4d). When the sensor moves at a uniform speed (200 $\mu\mathrm{m\ s^{-1}}$) along the direction from C_2 to C_4, the capacitance outputs of the four units are recorded in real-time. As shown in Fig. 4e and f, there is initially a stage of capacitance increase for

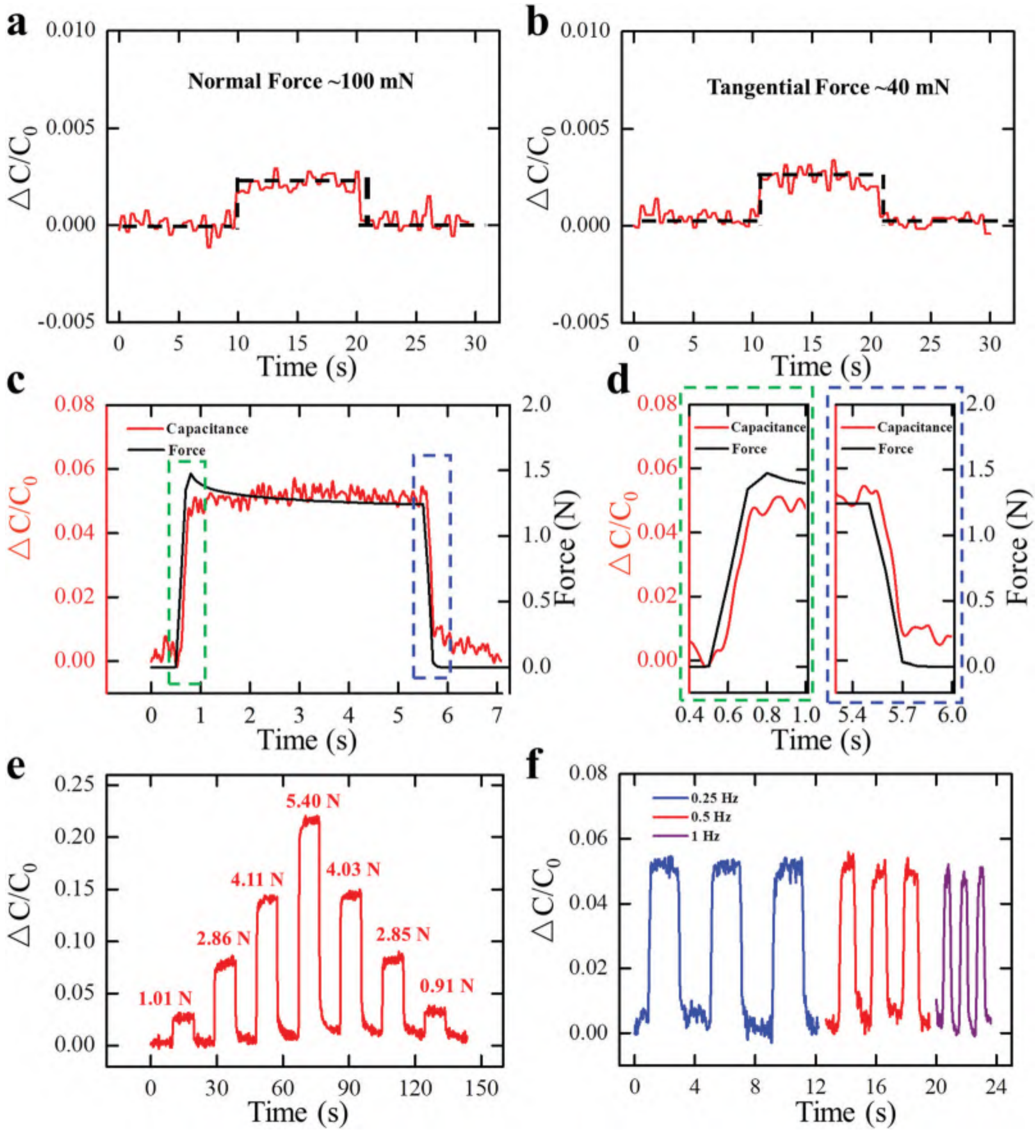

Fig. 3 (a and b) The minimum detectable forces in the normal and tangential directions. (c) Time-resolved capacitance changes with the sampling frequency of 200 Hz corresponding to a mechanical load of 1.3 N. (d) The response and recovery times are estimated from the falling and rising edges from the capacitive outputs in (c). (e) Time-resolved capacitance changes corresponding to dynamic mechanical loads varying from 0 to 5.4 N. (f) Time-resolved capacitance changes corresponding to dynamic mechanical loads with varying periodic frequencies of 0.25, 0.5 and 1 Hz.

all four units, corresponding to the generation of the porous elastomer deformation until its maximum by loading the tangential force component (the static stage in the blue region). Then, all the capacitance values reach a secondary stage of plateau after the PDiF sensor moves on the testing surfaces (sliding stage in the orange region). As expected, the capacitance change ratio of $\Delta C/C_0$ on the coarse surface is higher than that value on the smooth surface by nearly 9 folds. By calculating the differential capacitance changes in the opposite units, *i.e.*, C_{13} and C_{24}, we can estimate the shear forces as $\sim$0.5 N for the smooth surface, while $\sim$4 N for the coarse surface (Fig. 4g).

We have further investigated the slippage of objects with different surface roughness by using our PDiF sensor. As shown in Fig. 4h, the PDiF sensor is attached at the center of the palm of the first volunteer before the tests. Two different plastic sticks (Fig. 4i) are held in the hand with the PDiF sensor, and then slowly pulled out by a second volunteer. As for the stick with smooth surface (Stick #1 in Fig. 4i), the shear forces (F_x and F_y) measured by the PDiF sensors are featured with relatively smooth curves (up to 3.8 N, Fig. 4j). In contrast, as the stick with surface texture (Stick #2 in Fig. 4i) is pulled out, the force curves show remarkable saw-tooth variations (Fig. 4k). Collectively, these experiments validate that our sensor can sensitively differentiate the surface roughness, promising great applications in artificial sensation for robotics.

We have demonstrated high-resolution force-sensitive recognition of handwriting with the PDiF sensor. Fig. 5a illustrates how the PDiF-based "electronic pen" can be used to track the hand movements on a surface, with a real-time force profiling of the writing strokes. The capacitive changes of the four units

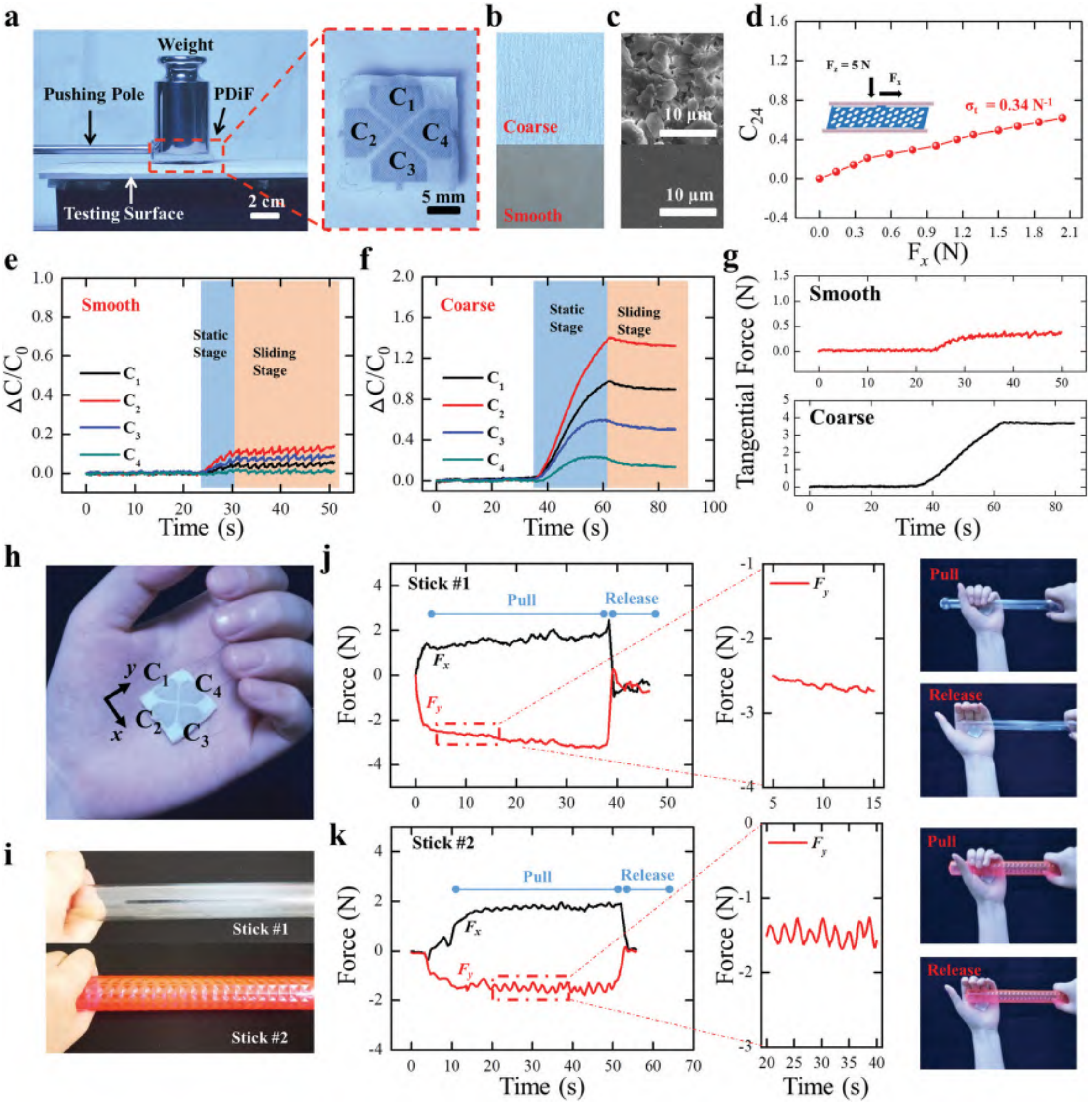

Fig. 4 Demonstrations for surface roughness detection using the PDiF sensor. (a) Illustration of the experimental setup to test the PDiF sensor placed between the plate surface and a weight of 500 g. (b and c) Photographs and SEM images of the coarse or the smooth plate surface. (d) Experimental calibration on the differential capacitance with the tangential forces under the constant load of 500 g. (e and f) Time-resolved capacitance changes of the four units when the PDiF sensor moved on these two different types of surfaces. (g) The calculated tangential forces as the sensor moved on the two types of surfaces. (h and i) The PDiF sensor is attached on the palm to detect the slippages of two sticks held in hand. (j and k) Real-time measurements of the tangential forces in both the *x*- and *y*-directions along the sensor surface, corresponding to different hand movements such as pulling and releasing the sticks.

are scanned and processed with a home-designed readout circuitry at a sampling rate of 5 Hz for each unit. The in-plane hand position can be calculated by continuously integrating the values of $C_x = \Delta C_2 - \Delta C_4$ and $C_y = \Delta C_1 - \Delta C_3$ by using an in-house developed tracking algorithm. Fig. 5b is the drawing of a "pentagram", in which the five sides are marked as "I", "II", "III", "IV", and "V" in different colors, according to the sequential order of the drawing strokes. Fig. 5c is a 3D plot of the reconstructed pentagram, with a force dependent variable (the value of C_{tot}) coordinating to the strokes. In addition, the time-resolved capacitive outputs of C_x and C_y at different time frames (#I–#V) of the pentagram drawing show characteristic patterns distinguishable from each other (Fig. 5d). For example, when the volunteer draws each side of the pentagram, the PDiF sensor experiences the force variations at different stages, leading to the modulated capacitive outputs: (1) in the blue regions, the normal force is applied on the sensor and the tangential force is increasing, simultaneously creating a scenario of static friction at the interface of the "electronic pen" and the writing board. (2) In the orange regions, as the "pen" moves on the surface of the board, the friction force retains a relatively constant level except for small fluctuations correlating to the volunteer's drawing habit as well as the surface roughness heterogeneity. (3) In the yellow regions, the "pen" rapidly pauses before the next

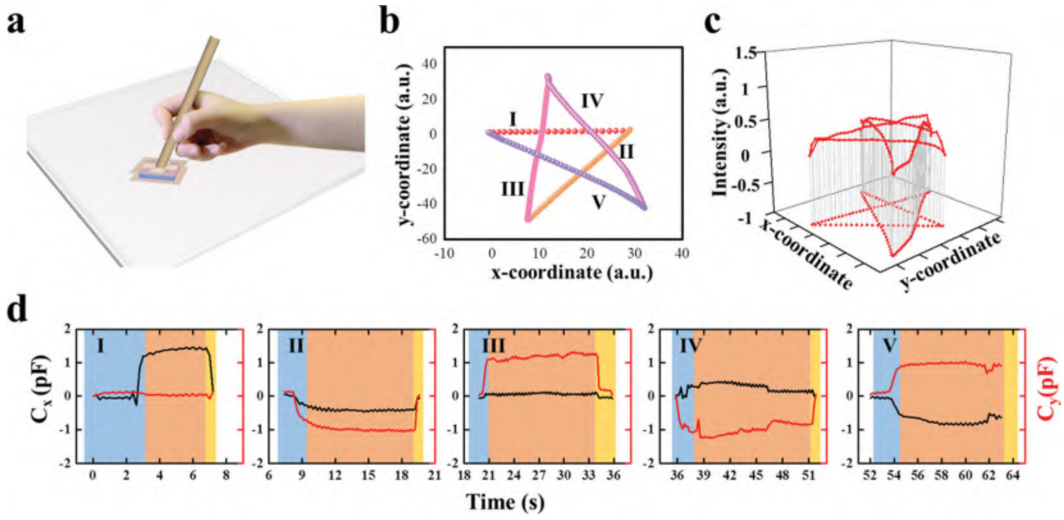

Fig. 5 Demonstrations for handwriting style recognition using the PDiF sensor. (a) Illustration of the experimental setup of the pen, the PDiF sensor, and the writing pad. (b) The drawing of a "pentagram" with five paths, *i.e.*, I, I, II, III, IV and V. (c) The reconstructed "pentagram" along with the corresponding variations of force intensity. (d) The time-resolved capacitive outputs C_x and C_y values. The capacitive outputs are split into five frames which are accordingly marked on the paths of the pentagram.

stroke, thus withdrawing the friction force. The values of C_x and C_y reveal the moving direction of the "pen" in all of the drawing strokes (Fig. 5d). For instance, in the orange region of frame #I, C_x is positive while C_y remains around zero, which indicates the moving direction towards x+ in the first stroke of the pentagram. According to a similar principle, in the orange region of frame #II, both the C_x and C_y are negative, corresponding to the movement toward the x- and y-direction. Interestingly, the rising rates for C_x (frame #I) and C_y (frame #III) in the blue regions are higher than those in the other frames (#II, #IV, and #V). This may reflect an individual drawing habit of the volunteer, who is adept at drawing horizontal and approximately vertical lines (the first and third strokes) instead of a tilted strip (the rest strokes in the pentagram). Fig. S6 in the ESI† presents the letters of the alphabet either in upper case or in lower case, which are reconstructed in the 3D plots after being written with the "electronic pen". Interesting force patterns, such as the valleys locally at the turning points and the plateaus corresponding to the relatively long strokes, can be identified as the force-indicative handwriting features of the volunteer.

Discussion

Many of the reports using porous materials, such as porous graphene oxide/PDMS,[17] interlocked Pt-coated polyurethane acrylate nanohairs[35] or interlocked carbon nanotube/PDMS microdomes[16] rely on the two-terminal resistive sensing mechanism. Those devices can usually measure the resistance changes induced by a single normal force or shear force separately. However, they cannot detect an arbitrary force containing any combination of three variable components with a two-terminal resistance signal. A few reports use microporous elastomeric sponge/foam as the dielectric material in a capacitive sensing mechanism.[39–41] However, those researchers only demonstrated the capacitive responses to the normal loads. They did not test their devices under the tangential loads, far from detecting any three-dimensional force.

There are two modes of decoupling from electrical outputs back to force components. Mode I: electrical signals can be measured by applying a single force component (*i.e.*, F_x, F_y, or F_z). Then, equations can be developed to quantify the relationship between the separate force components and electrical outputs. However, there is a lack of investigation as to whether the mathematical models can be generalized to decouple an arbitrary force containing two or three components. The reports[9,20,21] are classified as Mode I decoupling. Mode II is a significant promotion by solving this arbitrary force decoupling challenge. In order to address this issue, some researchers took neural network algorithms for 3D force decoupling, which was somehow limited to interpret the force–electric correlations in their devices.[34] In addition, G. Liang *et al.* developed a set of polynomial equations to decouple an arbitrary 3D force.[14] However, there is a major difference between Liang's report and our work in this manuscript. Their devices did not integrate porous structures in their dielectric material, thus missing the coupling enhancement contributed by the change in $\varepsilon/\varepsilon^0$. In comparison to those relevant reports in the literature (Table S1, ESI†), we have made a new contribution to this research field by solving the Mode II decoupling problem (arbitrary force analysis) with a porous dielectric elastomer sensor. Our decoupling method provides useful clues to understand how the components of the arbitrary contact force influence the elastomeric porous structures and determine the capacitance outputs in a synergistic manner.

The development of next-generation electronic signatures for identity verification demands multi-dimensional pattern recognition, while the force patterns in the handwritings can offer plenty of personalized characteristics for this purpose. The traditional handwriting devices, based on an accelerometer,[42] magnetic sensors[43] and optical sensors,[44] are able to reconstruct the writing graphics, but they nevertheless miss the critical information of the contact forces at the interface. A few reports integrate mechanochromic sensors inside the flexible "writing board" in order to simultaneously monitoring the writing path and the force/pressure intensity, which may be subject to the interference of ambient light during imaging.[45,46] Distinctly different from those sensing mechanisms in the literature, our capacitance-based PDiF sensor, as an "electronic pen", provides an alternative portable solution to 3D force-sensitive handwriting recognition in wearable electronics.

In summary, we have developed a wearable arbitrary contact force sensing device (PDiF sensor), featuring a porous elastomer with high permittivity. Benefiting from the porous structure, the mechanical-to-capacitance response is improved by three times compared to that with a solid structure. A mathematical model has been successfully built to address the complicated nonlinear relationship between the arbitrary contact forces and the capacitive outputs, mechanistically revealing the influence of the pore deformations on the contact force coupling. Our PDiF sensor is completely constructed from flexible materials (cotton and elastomer), allowing for the detection of the normal load by a sensitivity up to 0.16 N^{-1}, and the tangential load by 0.10 N^{-1}. The device has been applied in several scenarios for soft contact force detection, including surface roughness distinction, object slippage measurement, and handwriting recognition. The PDiF sensor integrating a porous elastomer offers a highly sensitive and flexible tactile sensing platform for the emerging wearable electronics.

Experimental section

A detailed description of the device fabrication and methods is available in the ESI.†

Conflicts of interest

There are no conflicts to declare.

Acknowledgements

This work was supported by the National Natural Science Foundation of China (61601317, 81371629, and 61622114); the Natural Science Foundation of the Jiangsu Province (BK20140052); the 111 Project; the Collaborative Innovation Center of Suzhou Nano Science and Technology; and the Priority Academic Program Development of Jiangsu Higher Education Institutions (PAPD).

Notes and references

1 T. Someya and M. Amagai, *Nat. Biotechnol.*, 2019, **37**, 382.

2 J. Li, R. Bao, J. Tao, Y. Peng and C. Pan, *J. Mater. Chem. C*, 2018, **6**, 11878.

3 Y. Ma, Y. Zhang, S. Cai, Z. Han, X. Liu, F. Wang, Y. Cao, Z. Wang, H. Li, Y. Chen and X. Feng, *Adv. Mater.*, 2020, **32**, e1902062.

4 H. C. Li, Y. J. Ma, Z. W. Liang, Z. H. Wang, Y. Cao, Y. Xu, H. Zhou, B. W. Lu, Y. Chen, Z. Y. Han, S. S. Cai and X. Feng, *Natl. Sci. Rev.*, 2020, **7**, 849.

5 G. Yu, J. Hu, J. Tan, Y. Gao, Y. Lu and F. Xuan, *Nanotechnology*, 2018, **29**, 115502.

6 Y. Gao, G. Yu, T. Shu, Y. Chen, W. Yang, Y. Liu, J. Long, W. Xiong and F. Xuan, *Adv. Mater. Technol.*, 2019, **4**, 1900504.

7 C. M. Boutry, M. Negre, M. Jorda, O. Vardoulis, A. Chortos, O. Khatib and Z. Bao, *Sci. Robot.*, 2018, **3**, eaau6914.

8 U. Kim, D. H. Lee, W. J. Yoon, B. Hannaford and H. R. Choi, *IEEE T Robot.*, 2015, **31**, 1214.

9 L. Viry, A. Levi, M. Totaro, A. Mondini, V. Mattoli, B. Mazzolai and L. Beccai, *Adv. Mater.*, 2014, **26**, 2659.

10 H. Zhang and M. Wang, *Soft Robot.*, 2016, **3**, 3.

11 Y. Ting, Suprapto, A. Nugraha, C. W. Chiu and H. Gunawan, *Sens. Actuators, A*, 2016, **250**, 129.

12 L. Xiong, G. Jiang, Y. Guo and H. Liu, *IEEE Sens. J.*, 2018, **18**, 3632.

13 T. Zhang, L. Jiang, X. Wu, W. Feng, D. Zhou and H. Liu, *IEEE/ASME Trans on Mech*, 2015, **20**, 1875.

14 G. Liang, Y. Wang, D. Mei, K. Xi and Z. Chen, *J. Microelectromech. Syst.*, 2015, **24**, 1510.

15 J. Z. Yin, V. J. Santos and J. D. Posner, *Sens. Actuators, A*, 2017, **264**, 289.

16 J. Park, Y. Lee, J. Hong, Y. Lee, M. Ha, Y. Jung, H. Lim, S. Y. Kim and H. Ko, *ACS Nano*, 2014, **8**, 12020.

17 C. Mu, Y. Song, W. Huang, A. Ran, R. Sun, W. Xie and H. Zhang, *Adv. Funct. Mater.*, 2018, **28**, 1707503.

18 S. Pyo, J. Choi and J. Kim, *Adv. Electron. Mater.*, 2018, **4**, 1700427.

19 M. Y. Cheng, C. L. Lin, Y. T. Lai and Y. J. Yang, *Sensors*, 2010, **10**, 10211.

20 J. A. Dobrzynska and M. A. M. Gijs, *J. Micromech. Microeng.*, 2013, **23**, 015009.

21 H. K. Lee, J. Chung, S. I. Chang and E. Yoon, *J. Microelectromech. Syst.*, 2008, **17**, 934.

22 H. K. Lee, J. Chung, S. I. Chang and E. Yoon, *J. Micromech. Microeng.*, 2011, **21**, 035010.

23 C. C. Kim, H. H. Lee, K. H. Oh and J. Y. Sun, *Science*, 2016, **353**, 682.

24 S. J. Kim, S. Mondal, B. K. Min and C. G. Choi, *ACS Appl. Mater. Interfaces*, 2018, **10**, 36377.

25 B. Nie, R. Huang, T. Yao, Y. Zhang, Y. Miao, C. Liu, J. Liu and X. Chen, *Adv. Funct. Mater.*, 2019, **29**, 1808786.

26 X. Shi, H. Wang, X. Xie, Q. Xue, J. Zhang, S. Kang, C. Wang, J. Liang and Y. Chen, *ACS Nano*, 2019, **13**, 649.

27 C. Lu, Y. Gao, G. Yu, M. Xu, J. Tan and F. Xuan, *Sens. Actuators, A*, 2018, **281**, 124.

28 S. Choi, S. I. Han, D. Kim, T. Hyeon and D. H. Kim, *Chem. Soc. Rev.*, 2019, **48**, 1566.

29 Y. C. Huang, Y. Liu, C. Ma, H. C. Cheng, Q. Y. He, H. Wu, C. Wang, C. Y. Lin, Y. Huang and X. F. Duan, *Nat. Electron.*, 2020, **3**, 59.

30 O. Atalay, A. Atalay, J. Gafford and C. Walsh, *Adv. Mater. Technol.*, 2018, **3**, 1700237.

31 M. Q. Jian, K. L. Xia, Q. Wang, Z. Yin, H. M. Wang, C. Y. Wang, H. H. Xie, M. C. Zhang and Y. Y. Zhang, *Adv. Funct. Mater.*, 2017, **27**, 1606066.

32 Z. Li, B. Zhang, K. Li, T. Zhang and X. Yang, *J. Mater. Chem. C*, 2020, **8**, 3088.

33 Y. Yue, N. S. Liu, W. J. Liu, M. A. Li, Y. A. Ma, C. Luo, S. L. Wang, J. Y. Rao, X. K. Hu, J. Su, Z. Zhang, Q. Huang and Y. H. Gao, *Nano Energy*, 2018, **50**, 79.

34 Y. Song, F. L. Wang and Z. Y. Zhang, *Micromachines*, 2018, **9**, 236.

35 C. Pang, G. Y. Lee, T. I. Kim, S. M. Kim, H. N. Kim, S. H. Ahn and K. Y. Suh, *Nat. Mater.*, 2012, **11**, 795.

36 Z. W. Ren, J. H. Nie, J. J. Shao, Q. S. Lai, L. F. Wang, J. Chen, X. Y. Chen and Z. L. Wang, *Adv. Funct. Mater.*, 2018, **28**, 1802989.

37 Q. K. Liang, W. N. Wu, G. Coppola, D. Zhang, W. Sun, Y. J. Ge and Y. N. Wang, *Robot. Comput.-Int. Manuf.*, 2018, **49**, 301.

38 W. Li, M. L. Zhan, Q. Y. Yu, B. Y. Zhang and Z. R. Zhou, *Biosurf. Biotribol.*, 2015, **1**, 278.

39 J. Yang, D. Tang, J. Ao, T. Ghosh, T. V. Neumann, D. Zhang, E. Piskarev, T. Yu, V. K. Truong, K. Xie, Y.-C. Lai, Y. Li and M. D. Dickey, *Adv. Funct. Mater.*, 2020, **30**, 2002611.

40 A. Chhetry, S. Sharma, H. Yoon, S. Ko and J. Y. Park, *Adv. Funct. Mater.*, 2020, **30**, 1910020.

41 D. Kwon, T.-I. Lee, J. Shim, S. Ryu, M. S. Kim, S. Kim, T.-S. Kim and I. Park, *ACS Appl. Mater. Interfaces*, 2016, **8**, 16922.

42 Y. L. Hsu, C. L. Chu, Y. J. Tsai and J. S. Wang, *IEEE Sens. J.*, 2015, **15**, 154.

43 X. Han, H. Seki, Y. Kamiya and M. Hikizu, *Precis. Eng.*, 2009, **33**, 37.

44 X. Zhang, Z. C. Ye, L. W. Jin, Z. Y. Feng and S. J. Xu, *IEEE Multimedia*, 2013, **20**, 85.

45 X. Wang, H. Zhang, R. Yu, L. Dong, D. Peng, A. Zhang, Y. Zhang, H. Liu, C. Pan and Z. L. Wang, *Adv. Mater.*, 2015, **27**, 2324.

46 S. Cho, S. Kang, A. Pandya, R. Shanker, Z. Khan, Y. Lee, J. Park, S. L. Craig and H. Ko, *ACS Nano*, 2017, **11**, 4346.